ADVANCED MATERIALS INTERFACES
www.advmatinterfaces.de

Binding Affinity and Conformational Preferences Influence Kinetic Stability of Short Oligonucleotides on Carbon Nanotubes

Ali A. Alizadehmojarad, Xingcheng Zhou, Abraham G. Beyene, Kevin E. Chacon, Younghun Sung, Rebecca L. Pinals, Markita P. Landry, and Lela Vuković**

DNA polymer-wrapped single-walled carbon nanotubes (SWNTs) finds a widespread use in a variety of nanotechnology applications. Molecular dynamics (MD) simulations and experiments are used to explore the relationship between structural conformation, binding affinity, and kinetic stability for short single-stranded oligonucleotides adsorbed on SWNTs. The conformation of 36 oligonucleotide sequences on (9,4) SWNT is computationally screened, where the polymer lengths are selected so the polymers can, to a first approximation, wrap once around the SWNT circumference. The identified conformations can be broadly classified into "rings" and "non-rings." Then, 2D conformational free energy landscapes for selected sequences are obtained by temperature replica exchange calculations. Propensity for "ring" conformations are driven primarily by sequence chemistry and the ability of the polymer to form compact structures. However, ring-formation probability is found to be uncorrelated with free energy of oligonucleotide binding to SWNTs (ΔG_{bind}). Conformational analyses of oligonucleotides, computed free energy of binding of oligonucleotides to SWNTs, and experimentally determined kinetic stability measurements show that ΔG_{bind} is the primary correlate for kinetic stability. The probability of the sequence to adopt a compact, ring-like conformation is shown to play a secondary role that still contributes measurably and positively to kinetic stability.

1. Introduction

Single walled carbon nanotubes (SWNTs) comprise a key component of many new nanotechnology applications for sensing, biological imaging, electronics, and gene delivery, among others.[1–11] Noncovalent polymer adsorption is a widely used method to confer and optimize desired functionalities to SWNTs, while solubilizing them in aqueous environments. A variety of polymers, which when adsorbed form a "corona phase" on the surface of SWNT, have been used for SWNT functionalization, including nucleic acids, peptides, peptoids, lipids, surfactants, and others.[12–20] Among those, nucleic acid-functionalized SWNTs in particular were found to have a number of technologically useful and important applications.[5,10,21–24] This variety of polymers and the ease of functionalization through noncovalent adsorption provide a great opportunity for rational design of SWNT conjugates for specific applications. However, rational design methodologies for corona phase engineering would benefit from a systematic body of knowledge about how individual polymer properties, such as polymer length, sequence, and chemistry, relate to structural and kinetic properties of the resulting corona phase. As the polymer corona cannot be directly visualized with atomic resolution in experiments, important characteristics of the corona phase, such as structural arrangement of polymers, corona thickness, dynamics of assembled polymers on different timescales, kinetic stability and interactions with other molecules present in the suspension, have to be inferred from experiments with limited resolution.[25–29]

A. A. Alizadehmojarad, K. E. Chacon, Prof. L. Vuković
Department of Chemistry and Biochemistry
University of Texas at El Paso
El Paso, TX 79968, USA
E-mail: lvukovic@utep.edu

X. Zhou, Dr. Y. Sung, R. L. Pinals, Prof. M. P. Landry
Department of Chemical and Biomolecular Engineering
University of California
Berkeley, CA 94720, USA
E-mail: landry@berkeley.edu

The ORCID identification number(s) for the author(s) of this article can be found under https://doi.org/10.1002/admi.202000353.

DOI: 10.1002/admi.202000353

Dr. A. G. Beyene
Janelia Research Campus
Howard Hughes Medical Institute
Ashburn, VA 20147, USA

Prof. M. P. Landry
California Institute for Quantitative Biosciences, QB3
University of California
Berkeley, CA 94720, USA

Prof. M. P. Landry
Innovative Genomics Institute
Berkeley, CA 94702, USA

Prof. M. P. Landry
Chan-Zuckerberg Biohub
San Francisco, CA 94158, USA

An alternative and a powerful way to characterize the corona phase includes computational modeling approaches, such as classical molecular dynamics (MD) simulations, which enable atomic resolution on the timescale of hundreds of nanoseconds.[1,2,29–32] Yet, as reorganization of long polymers on SWNT surfaces occurs on a timescale of several nanoseconds, determining most probable equilibrium distributions of polymers in the corona phase necessitates enhanced sampling approaches, such as temperature replica exchange MD (T-REMD) simulations.[33] Complete free energy landscapes and equilibrium distributions of select representative polymers, such as single DNA sequences, on the SWNT surface were determined in prior studies.[2,30,34] While the number of systems sampled in simulations has typically been small, limited to several sequences at most, investigating a larger number of systems recently became more computationally feasible.

Generating extended sets of data from systematically sampled atomistic resolution simulations could open attractive routes for developing predictive frameworks for corona phase design, which could overcome the present severe limits of ab initio predictions of polymers with specific functions, such as SWNT or analyte recognition. Several recent experimental studies already address the lack of big data in the polymer-functionalized SWNT field in general, utilizing high-throughput approaches to discover polymers (nucleic acid sequences) which can recognize specific chiralities of SWNTs or sense particular analytes, such as serotonin.[35,36] In the present paper, we select an extended set of related nucleic acid polymers, which vary in sequence but have similar short lengths, and combine extended atomistic-resolution computational screening (MD, T-REMD simulations) with lower-resolution experimental screening (kinetic stability surfactant displacement experiments) to relate and generalize the relationships among structural conformation, binding affinity, and kinetic stability of short oligonucleotides adsorbed on SWNTs.

2. Results and Discussion

2.1. Screening Conformations of Circumference-Matching Nucleic Acid Polymers on (9,4) SWNTs

In a previous study,[2] we reported results from molecular dynamics simulations, showing that the oligonucleotide sequence, $(GT)_6$, formed semi-ordered, ring-like structures when adsorbed on (9,4)-SWNT but did not do so when adsorbed on (6,5)-SWNT. Numerous studies have previously investigated surface conformations of oligonucleotides adsorbed on SWNTs and identified helical structures as the general predominant form. The ring-like structural motifs were unique to our study and suggested that short oligonucleotides adsorbed on bigger diameter SWNT may form ordered ring-like structures that render unique photophysical and functional properties to the oligonucleotide-SWNT hybrid structure.

Here, we first explore relationships among sequence chemistry, binding affinity, and surface free energy landscape to gain better understanding of ring-forming sequences and identify physical rules that underpin their formation. Toward this end, we screened the conformations of 36 short single-stranded nucleic acids on (9,4) SWNTs through single-trajectory equilibrium MD simulations. The sequences screened included 10-, 11-, and 12-nucleotide (nt) long ssDNA and ssRNA, whose lengths, to a first approximation, matched the circumference of the (9,4)-SWNTs (**Figure 1**a; Table S2, Supporting Information). These nucleic acid strands were initially equilibrated with left-handed helix configurations around (9,4) SWNTs in 0.1 M NaCl aqueous solution. After minimization and brief (2 ns) equilibration of the ions around the restrained nucleic acids and SWNTs, the nucleic acids were released from restraints and equilibrated for an additional 80 ns.

Figure 1a and Table S2 (Supporting Information) summarize the results of the screening performed and quantify the probability of ring formation. While ≈31% of the sequences had a strong probability (>0.15) to form rings around (9,4) SWNTs, ≈40% of the sequences had a low probability (<0.05) or were not observed to form ring conformations. The remaining 28% of the sequences screened showed intermediate probability to form ring conformations around (9,4) SWNTs. Multiple sequences adopted ring conformations, including the previously examined $(GT)_6$.[2] Several independent MD simulations were performed for several sequences, in some of which C_{12} ssDNA formed the most stable rings that exhibited a perpendicular arrangement with respect to the SWNT axis. A variety of ring-forming conformations were observed, where the rings were either perpendicular to or tilted with respect to the SWNT axis. The rings formed via hydrogen bonding between 3′- and 5′-end nucleotides, with hydrogen bonds forming between polar and hydrogen atoms on either backbones, sugar rings, or bases of these nucleotides. Many different hydrogen bonds are observed to stabilize the rings on SWNTs, unlike the well-defined covalent bonding in circular nucleic acids.[37] Some sequences, including T_{12}, did not form any ring conformations in the screening simulations. To further confirm the existence of ring- versus helix-forming structures on SWNT, we performed high-resolution TEM microscopy of two previously reported ring- and helix-forming structures, short $(GT)_6$ and long $(GT)_{15}$ molecules, respectively, on SWNT surfaces. TEM images suggest the predicted ring and helix conformations (Figure S1, Supporting Information) for $(GT)_6$ and $(GT)_{15}$ molecules, as had been structurally suggested by our prior MD studies.[2]

Several related short ssRNA sequences were also screened for ring formation (Table S2, Supporting Information). These ssRNA sequences displayed different behavior from ssDNA sequences. Namely, ssRNA sequences formed either no ring structures ($(CU)_5$) or had a large probability to form transient rings that are significantly more tilted with respect to SWNT axes than ssDNA sequences, with 3′- and 5′-end nucleotides bonding transiently via hydrogen bonding ($(CU)_5UU$, $(CU)_6$, and $(CU)_5C$) (Table S2, Supporting Information). Transience of ssRNA ring structures in comparison to ssDNA ring structures was noted in 3D scatter plots of end-to-end distances and RMSD values of all structures with respect to the reference structure for each time frame (Methods). For ssRNA trajectories, the points representing rings in the scatter plots did not form well separated clusters, whereas for most of the ssDNA

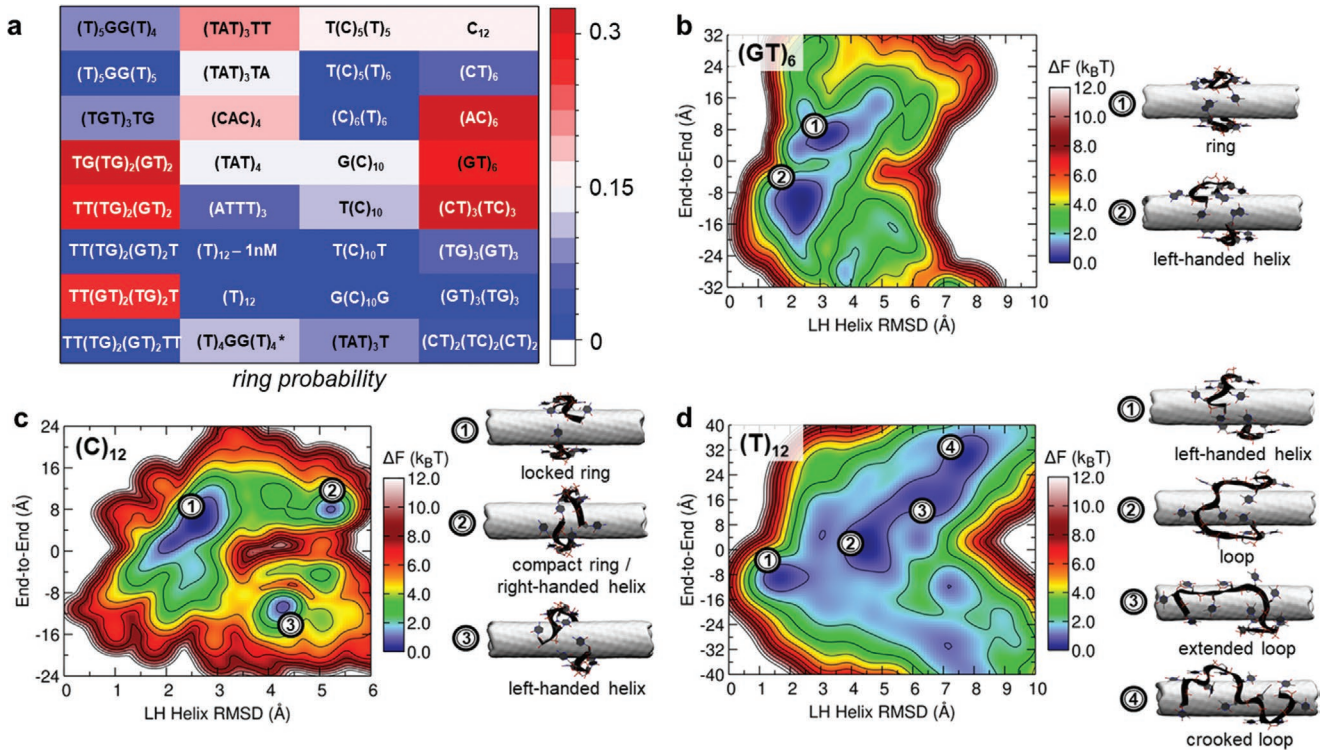

Figure 1. Single-stranded nucleic acid conformations on (9,4) SWNT at 300 K. a) Screening of 32 sequences for ring conformation probabilities on (9,4) SWNTs in short single trajectory MD simulations at 300 K. b) Free energy landscape of $(GT)_6$ on (9,4) SWNT in T-REMD calculation at 300 K. $(GT)_6$-SWNT has two free energy minima, corresponding to 1) ring and 2) left-handed helix conformations. c) Free energy landscape of C_{12} on (9,4) SWNT in T-REMD calculation at 300 K. C_{12}-SWNT has free energy minima corresponding to 1) locked ring, 2) compact ring/right-handed helix, and 3) left-handed helix conformations. d) Free energy landscape of T_{12} on (9,4) SWNT in T-REMD calculation at 300 K. T_{12}-SWNT has four free energy minima corresponding to 1) left-handed helix, 2) loop, 3) extended, and 4) crooked loop conformations.

trajectories the points corresponding to ring structures formed clusters. The presence of the ribose sugar oxygen on ssRNA was previously correlated to the diminished stability of ssRNA on SWNTs in comparison to ssDNA.[38] A similar effect could potentially be contributing to the lower stability of ssRNA rings in comparison to ssDNA rings.

2.2. Free Energy Landscapes of Circumference-Matching Oligonucleotides on (9,4) SWNTs

Based on the screening reported in Figure 1a, multiple nucleic acid sequences with different ring-formation behavior in short single trajectory MD simulations were selected for detailed investigation based on better conformational sampling.[2,34] While single trajectory MD simulations allow quick sampling of many systems, oligonucleotide conformations explored in these simulations can be limited and dependent on the choice of the initial structure. These limitations can be overcome by the use of T-REMD simulations, which at significantly higher computational cost permit detailed explorations of free energy landscapes that may not be fully sampled in single trajectory MD simulations.[2,34] T-REMD simulations are considered to provide extensive sampling of the entire ensemble of conformations of short oligonucleotides[34] similar in length to those examined in the present study. Here, $(GT)_6$, C_{12}, $(CT)_6$, $(CAC)_4$, $(TG)_3(GT)_3$, and $(CT)_3(TC)_3$ ssDNA sequences (weak to strongly ring-forming in single trajectory MD simulations), T_{12} and $(GT)_3(TG)_3$ (not ring forming in single trajectory MD simulations) ssDNA sequences, and $(CU)_6$ and $(CU)_5UU$ (both ring-forming) ssRNA sequences were examined in T-REMD calculations. The free energy landscapes and the structures representative of the free energy minima for these sequences obtained from T-REMD calculations at T = 300 K are shown in Figure 1b–d and Figures S2 and S3 (Supporting Information). All the studied sequences showed multiple free energy minima, corresponding to different representative surface structures. The sequences with significant free energy minima basins that represent ring conformations include $(GT)_6$ (≈40% of the ensemble), C_{12} (≈90% of the ensemble), $(CT)_3(TC)_3$ (≈90% of the ensemble, localized and ordered), and $(GT)_3(TG)_3$ (≈75% of the ensemble). Interestingly, single-trajectory MD simulations did not identify $(GT)_3(TG)_3$ as a ring-forming sequence. The other free energy minima these sequences exhibited corresponded to left-handed and right-handed helices.

Three related ssDNA and ssRNA sequences ($(CT)_6$, $(CU)_6$, and $(CU)_5UU$ sequences) were also examined (Figure S2, Supporting Information). These related sequences all show high ring-forming propensity and have free energy landscapes with similar features in which the free energy minima exhibit elongated diagonal basins. The similar features of the free energy minima for both ssDNA and ssRNA sequences indicate that

both base identity and order strongly influence favored conformations of oligonucleotides.

Two sequences, T_{12} and $(TG)_3(GT)_3$, showed no or weak ring minima, but $(TG)_3(GT)_3$ had a strong minimum associated with compact left-handed helix structures. The latter sequence, $(TG)_3(GT)_3$, was classified as a ring-forming sequence in the single-trajectory MD screening calculations. The two specified sequences were also the only sequences that exhibited flexible and disordered loop structures, which did not wrap SWNTs around the circumference.

The observation that some sequences did not exhibit rings in screening simulations, but did so in T-REMD calculations that have improved conformational sampling, and vice versa, as especially observed for $(GT)_3(TG)_3$ and $(TG)_3(GT)_3$, indicates that 12-nt ssDNA molecules do not fully explore their conformational space on SWNTs in single trajectory equilibrium MD simulations on the timescale of ≈100 ns.

2.3. Ring Conformations Form Compact Structures

Since many free energy minimum structural ensembles obtained in T-REMD calculations contained ring structures (Figure 1b–d; Figures S2 and S3, Supporting Information), these structures were analyzed to identify structural properties that could characterize them. Visually, two factors seem to be correlated with ring conformations. First, ring conformations often exhibit kinks in the backbone, as shown schematically in the inset of **Figure 2**a. With such a backbone, the ring structure appears to be more compact than other types of conformations observed, such as helical structures (intermediately compact) and loops (least compact). In ring structures, hydrogen bonding (such as between bases or backbones of (n, n + 2) nucleotides, shown schematically in the inset of Figure 2a) and bound ions appear to stabilize the compact conformations.

To quantify if ring conformations on average have a more compact backbone with a zig–zag structure (kinks) in it, we calculated the angles between phosphorus (P) atoms of three neighboring phosphate groups, averaged over all triplets of P-atoms on neighboring nucleotides and over all the structures in the specified free energy minimum basins. The average angles we obtained, whose values range from ≈95° to ≈125°, are shown in Figure 2a. For most of the sequences examined, ring conformations exhibit the smallest angles among the major conformations observed, and therefore the sharpest turns (kinks) in the backbone.

Ring conformations also appeared to be more compact than other conformations due to the presence of ions and potentially hydrogen bonds between (n, n + 2) nucleotides. The nucleic acids occasionally form pockets in which ions are stabilized for long times, as reported in our previous study.[2] The average numbers of ions at close distance (within 4 Å) from nucleic acids of different sequences and in different conformations are shown in Figure 2b. The average number of sodium ions ranged from ≈2.6 to ≈6.6 and is strongly sequence dependent. In several sequences, $(GT)_6$, C_{12}, and $(TG)_3(GT)_3$, ring conformations had a higher number of sodium ions nearby on average than other conformations.

Representative structures of two sequences that had a strong propensity, C_{12}, and no propensity, T_{12}, for ring formation were examined by means of contact maps, shown in **Figure 3**. The opacity of color in contact maps represents the probability of nucleic acid pairs being found within 4.5 Å of each other. Figure 3a shows contact maps of structural ensembles corresponding to ring, right-handed, and left-handed helix conformations of C_{12}. For all three conformations, each nucleotide has four highly

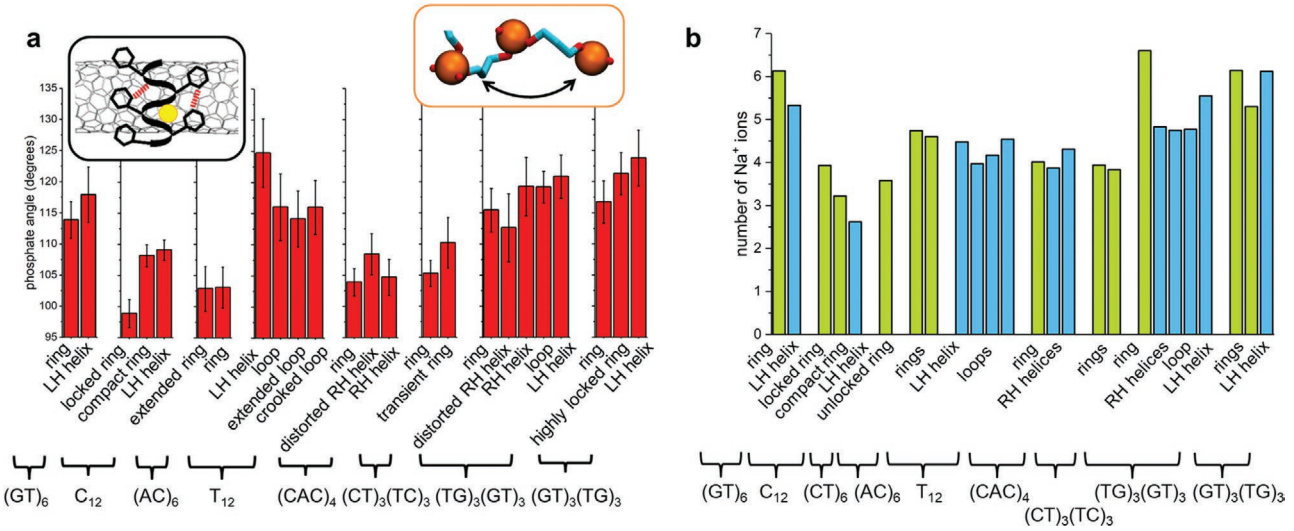

Figure 2. Analysis of conformational ensembles. a) Phosphate angles (orange inset) in major nucleic acids conformations, averaged over all P-atom triplets and over all the structures within the specified free energy minimum basins, determined from T-REMD calculations at 300 K. Black inset: a scheme of the ring conformation, exhibiting zig–zag structure of the backbone, which is stabilized via (n, n + 2) hydrogen bonding and bound ions. b) Average number of sodium ions within 4 Å of nucleic acids examined, averaged over all the structures in free energy minimum basins, determined from T-REMD simulations at 300 K. Bars corresponding to ring conformations are shown in green, while bars corresponding to other conformations are shown in blue. Abbreviations LH and RH refer to left-handed and right-handed helices. Full values and names of conformations are given in Table S3 in the Supporting Information.

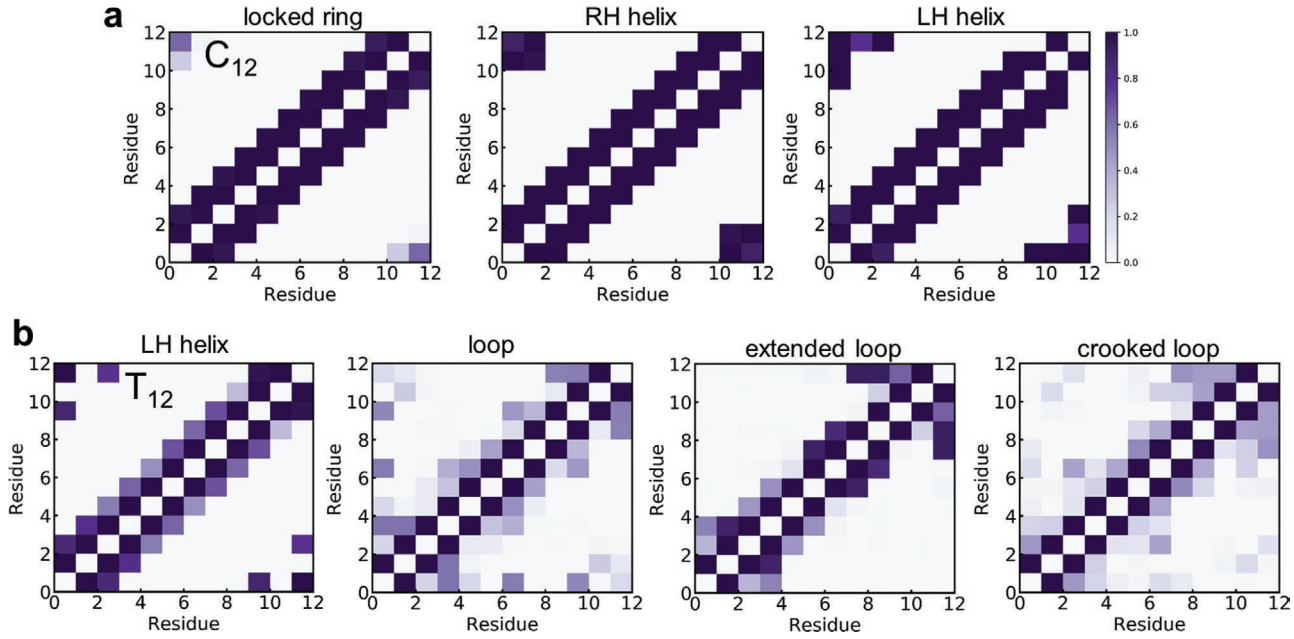

Figure 3. Contact maps of C_{12} and T_{12} ssDNA, where the structures are separated according to their free energy minimum basins. The structural ensembles of ssDNA molecules on (9,4) SWNTs were extracted from REMD simulations at 300 K. Abbreviations LH and RH refer to left-handed and right-handed, respectively.

probable neighbors: two nucleotides that are covalently linked to it, and two nucleotides that are its second neighbors ((*n*, *n* + 2) interactions). The second-neighbor interactions are prominent due to compactness of ring and helical conformations. In ring conformations, the first and the last nucleotides are observed to interact while clasping the ring. In helical conformations, more nucleotides at 3′- and 5′-ends tend to interact.

Figure 3b shows contact maps of structural ensembles corresponding to left-handed helix and three different loop conformations of T_{12}. Contact maps of T_{12} exhibits very different features from C_{12} maps. In T_{12}, each nucleotide primarily interacts with its nearest covalently linked neighbors and exhibits much weaker interactions with second neighbors ((*n*, *n* + 2)). In T_{12}, there are also more interactions of nucleotides with their nonimmediate neighbors.

Interestingly, there is no correlation between the ssDNA composition (including purine, C-nt, T-nt, and G-nt fractions in ssDNA) and the ring formation propensity, as shown in Figure S4 in the Supporting Information. Also, we examined if molecules in conformations in ring basins have contact areas with SWNTs that are distinct from conformations in other basins (Figure S5, Supporting Information). While contact area of C_{12} ring conformations was higher by ≈100 Å^2 compared to other conformations, $(GT)_6$ ring conformations exhibited contact areas smaller by ≈60 Å^2 than the left-handed helix conformations. Therefore, contact area of ssDNA with SWNT did not seem to be correlated with the ring conformation.

2.4. Free Energy Landscapes at Low Ionic Strength

Conformations of DNAs on SWNTs are predicted to have a pronounced dependence on the ionic strength.[26] Therefore, we examined how the free energy landscape of two representative sequences, C_{12} and T_{12}, were affected by lowering the ionic strength. The free energy landscapes for these sequences at 150×10^{-3} and 1×10^{-3} M NaCl solutions are shown in **Figure** 1c,d and **4**, respectively. We found that the free energy minima are in roughly the same parts of the reaction coordinate space for both ionic solutions. However, relative populations of these minima are shifted. For C_{12}, minimum 1 (ring) becomes less populated, minimum 2 (right-handed helix) becomes more populated, and minimum 3 (left-handed helix) becomes shallower and broader, likely due to more pronounced electrostatic repulsion between phosphate groups. For T_{12}, locations of free energy minima are also similar for both ionic solutions. However, in 1×10^{-3} M NaCl, minima were less separated by free energy barriers (transitions between different minima are more likely). In addition, other smaller local minima observed in 150×10^{-3} M NaCl become more pronounced in 1×10^{-3} M NaCl. Since free energy minima are located in roughly the same parts of the reaction coordinate space for both ionic solutions, our results seem to indicate that free energy landscapes for short ssDNA are more sequence-dependent than solution ionic strength dependent. However, other intermolecular (inter-ssDNA) phenomena may emerge in low NaCl concentration solutions, which were not captured in the simulations performed.

2.5. Kinetic Stability of Short Oligonucleotides on SWNTs in Experiments

To explore the relationship between sequence chemistry and kinetic stability, we performed surfactant displacement experiments on twelve screened sequences. Previous studies have

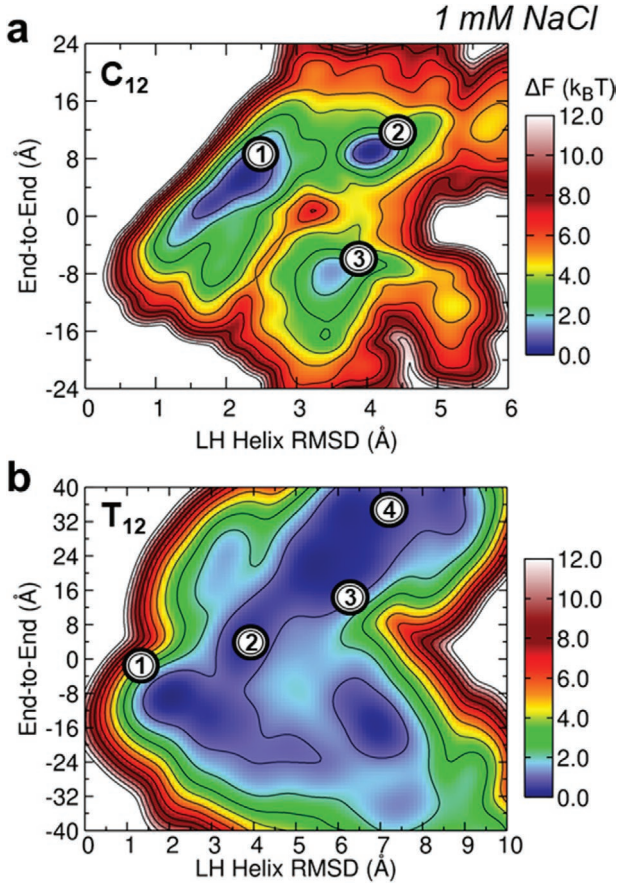

Figure 4. Free energy landscapes of a) C_{12} and b) T_{12} ssDNA on (9,4) SWNTs at 300 K, in 1×10^{-3} M NaCl aqueous solutions. The labels indicating free energy minima and their representative structures correspond to the labels shown in Figure 1. Free energy landscapes for the same sequences in 150×10^{-3} M NaCl aqueous solutions are shown in Figure 1.

shown that high affinity surfactants like sodium cholate (SC) can displace SWNT surface-adsorbed ssDNA.[39–41] We leveraged SC affinity for the SWNT surface to obtain an experimental readout for the relationship between sequence chemistry and kinetic stability of the adsorbed species. Toward this end, we added SC to ssDNA-SWNT suspensions to displace the oligonucleotides adsorbed to the SWNT surface. All sequences display a blue-shift of center peak wavelengths, where each peak corresponds to a different chirality, suggesting displacement of the surface-adsorbed oligonucleotides by SC. **Figure 5**a,b shows the time-resolved solvatochromic shift of the (9,4) peak monitored over 300 s. Upon SC addition, the (9,4) peak shifts toward 1116 nm, which is the (9,4) peak of SC-suspended SWNT, suggesting that SC has displaced most of the surface-adsorbed oligonucleotides. We identified four sequences that displayed minimal wavelength shift, exhibiting a change of approximately 1 nm over the time period monitored. We hypothesize that the extent of the blue-shift reflects the degree of displacement by SC and eventual surfactant surface coverage, and the speed with which the shift occurs indicates the ease of displacement of the oligonucleotide.

To quantitatively analyze the kinetics of the process, we assumed the temporal dynamics follow a first-order kinetic model and fit the experimental data using least squares regression, from which decay time constants were determined (Figure 5c). Here, larger time constants correlate with a slower blue-shift. Four sequences, $(GT)_6$, $TC_{10}T$, $(GT)_3(TG)_3$, and $(TG)_3(GT)_3$, were found to have time constants at least an order of magnitude larger than the rest. These four sequences also exhibited minimal blue-shifting (Figure S6, Supporting Information). We hypothesize that the relative value of the time constants and extent of blue shift reflects the relative kinetic stability of the oligonucleotide sequences on the SWNT surface, with a higher time constant representing a more robust stability of the oligonucleotide adsorbed to the SWNT.

We validated the relationship between ssDNA stability and ssDNA desorption from SWNT by performing a SWNT corona ligand tracking assay.[28] We hypothesize that ssDNA sequences that show shorter SC-induced time constants are likelier to desorb from the SWNT surface altogether. To determine the degree of SC-induced desorption of ssDNA, we tracked the ssDNA proximity to the SWNT with fluorophore quenching. We acquired four sequences of ssDNA, $(GT)_6$, C_{12}, $(TAT)_4$, and T_{12}, with a Cy5 fluorophore (ex/em 664/668 nm) on the 3′ end. The Cy5 fluorophore is initially quenched when ssDNA is on the SWNT surface, and the fluorescence increases in intensity upon ssDNA desorption from the SWNT.[28] SC was added to ssDNA-Cy5-SWNT in a well plate and the Cy5 fluorescence was measured over time to monitor the degree of ssDNA desorption. All sequences showed an increase in fluorescence over time (Figure S7, Supporting Information), consistent with the prediction that upon the addition of SC, ssDNA is displaced from SWNT surface. Out of the four sequences tested, T_{12} displayed the largest fluorescence fold increase and $(GT)_6$ the smallest, suggesting that T_{12} had the highest degree of desorption. Overall, we find that a larger SWNT fluorescence increase correlates with a smaller solvatochromic shift time constant (Figure 5d), suggesting that the solvatochromic shift is a good indicator of the degree of ssDNA desorption from the SWNT. A larger time constant is associated with slower desorption, which agrees with the earlier hypothesis that the speed and extent of the solvatochromic shift correlates with ssDNA kinetic stability. As a control, when SC is added to a solution of dye-labeled ssDNA, only marginal increases in fluorescence were observed, likely driven by changes in solvent dielectric constant (Table S4, Supporting Information); the experiments suggest that the difference in both the magnitudes and time constants measured with the solvatochromic shift assay are due to differences in the affinities of different ssDNA sequences for the SWNT, and not a function of SC interaction with the ssDNA (Figure S8, Supporting Information). Therefore, this corona ligand tracking assay is consistent with data collected from SWNT fluorescence alone and the results in sum offer an experimental insight into kinetic stability of adsorbed species.

Next, we examined the influence of theoretical oligonucleotide binding affinity and its favored conformation on its experimental kinetic stability on SWNT. Oligonucleotide binding and conformational changes on SWNTs, depicted in **Figure 6**c, are driven by its search for the free energy minimum state on SWNTs. We hypothesized that both the binding affinity and the nature of the favored conformation may affect the ease of displacement of oligonucleotides on

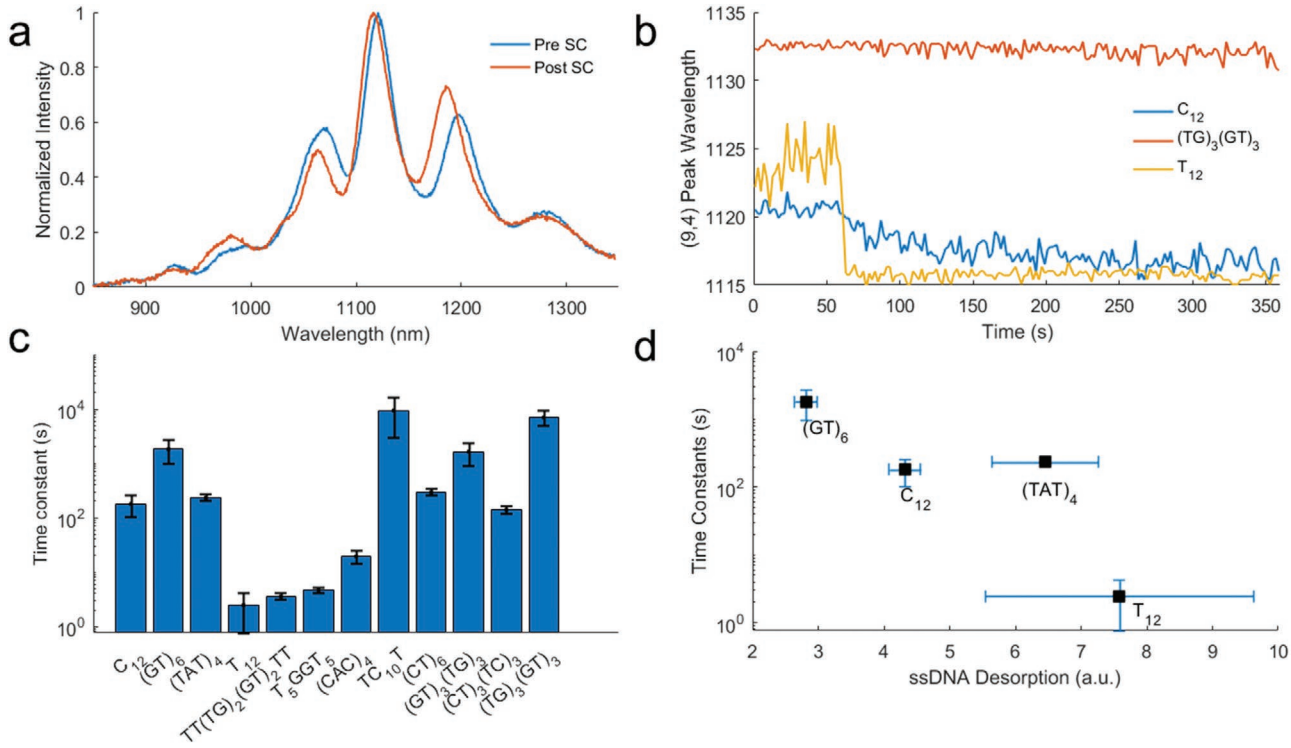

Figure 5. Sodium cholate (SC) induced solvatochromatic shift is dependent on ssDNA sequence. a) Addition of 0.1% SC induces a solvatochromic shift in C_{12}-SWNT fluorescence. b) Time resolved fluorescence measurements of C_{12}-SWNT, $(TG)_3(GT)_3$-SWNT, and T_{12}-SWNT upon addition of SC as indicated by arrow. The degree of the solvatochromic shift is sequence dependent. c) Time constants of the solvatochromic shift are representative of time needed for ssDNA to be displaced from the surface by SC surfactant. d) Larger solvatochromic shift time constants are correlated to lower degrees of ssDNA desorption.

the SWNT surface by surfactants and therefore its kinetic stability. To estimate the binding affinity of each sequence to SWNTs, a simple model was prepared based on summation of single nucleotide binding free energies to SWNTs for all the nucleotides within single strands. The single nucleotide binding free energies are based on the values reported by Johnson et al.,[34] estimated for a system containing (5,5) SWNT (*A*: –11.3 kcal mol^{-1}, *G*: –13.145 kcal mol^{-1}, *C*: –6.92 kcal mol^{-1}, *T*: –11.76 kcal mol^{-1}). The estimated binding affinities of several sequences are reported in Figure S9 in the Supporting Information.

Figure 6a shows experimentally determined time constants of selected ssDNA sequences, extracted from Figure 5, versus their estimated free energies of binding to SWNTs, ΔG_{bind}, extracted from Figure S9 in the Supporting Information. Clear correlations are observed between ΔG_{bind} and the time constant, i.e., the kinetic stability, for all the sequences shown, except for an outlier T_{12} sequence, which has a large ssDNA-SWNT binding free energy (ΔG_{bind} = –141.1 kcal mol^{-1}), but a low kinetic stability. The observed correlations confirm that the ease of displacement of oligonucleotides on SWNTs by surfactants depends on how strongly the oligonucleotides bind to SWNT, as measured by ΔG_{bind}.

To examine if the nature of the favored conformation of the oligonucleotide also affects its kinetic stability, the relationship among ΔG_{bind}, favored conformation of the sequence, and the kinetic stability of selected sequences is plotted in Figure 6b. The favored conformations are classified as either ring/helix, in which the oligonucleotides are "ordered" via strong (n, n + 2)-nucleotide interactions, or loop conformations, in which oligonucleotides are more disordered. Again, Figure 6b confirms that the binding affinity of the sequence to SWNTs has a clear correlation to its kinetic stability. The favored conformation then has a secondary influence on kinetic stability: the "ordered" conformations are somewhat correlated with slightly increased kinetic stability of sequence, as seen, for example, for sequences with weaker affinity to SWNTs (sequences with a large fraction of C-nucleotides, $\Delta G_{bind} > -120$ kcal mol^{-1}). We note that intermolecular interactions are not accounted for in the analysis, but could play an important role and lead to further modulation or a larger change in kinetic stability.

3. Conclusion

In conclusion, we have expanded the understanding of short oligonucleotide sequences that form ring-like structural motifs when adsorbed on SWNTs. Based on this work, we conclude that ring structural motifs on SWNTs emerge as a consequence of the oligonucleotide's ability to form intramolecular hydrogen bonds, in particular between (n, n + 2) nucleobases and between bases at the 3′ and 5′ ends of the polymer. The ring conformation is favored in sequences that are best able to accommodate sharp bends in their phospho-diester backbone.

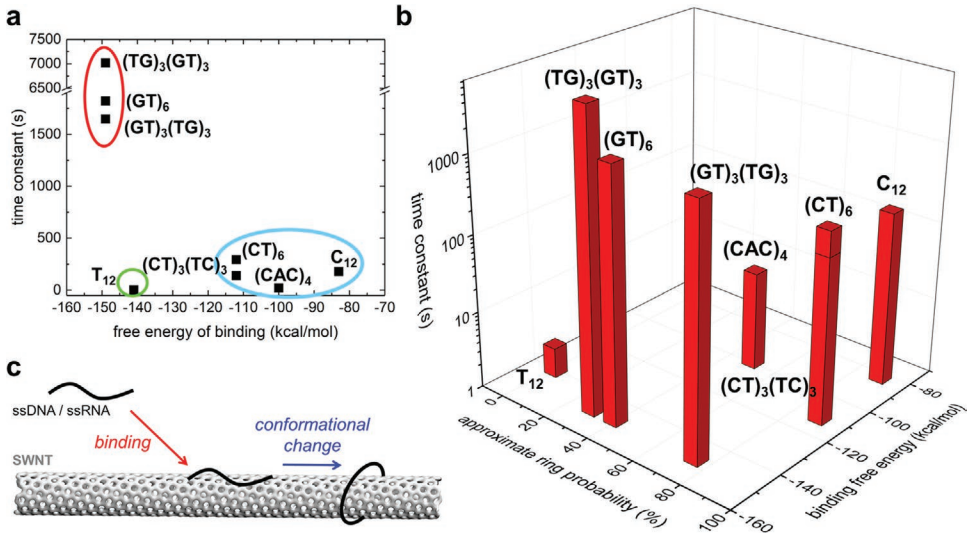

Figure 6. Correlations between computational and experimental data. a) Experimentally determined time constants of select ssDNA sequences versus their estimated free energies of binding to SWNT (Figure S9, Supporting Information). b) Experimentally determined time constants of select ssDNA sequences versus their estimated free energy of binding to SWNT (Figure S9, Supporting Information) and their approximate probability to form ring conformation. The bars for $(CT)_3(TC)_3$ and $(CT)_6$ overlap, with $(CT)_6$ corresponding to the taller bar. c) A scheme of the processes associated with the adsorption of oligonucleotides to (9,4) SWNTs: initial binding of oligonucleotides, followed by conformational changes between favorable conformations, revealed in the free energy landscapes. For $(TG)_3(GT)_3$, approximate ring probability is estimated from the structures in both ring and compact left-handed helix (partly) basins.

Ring-formation propensity is therefore likely an emergent property driven by the chemistry of the constituent bases and base stacking interactions with the SWNT surface. Our work however did not identify particular chemical trends (for example, purine versus pyrimidine content) that reliably correlated with the formation of rings. Experimentally, we explored kinetic stability of the surface-adsorbed polymers using a surfactant displacement assay. We identified that computed estimates of ΔG_{bind} are the primary correlates of experimentally measured stability. However, in sequences with unfavorable free energy of adsorption (more positive ΔG_{bind}), ring structures contributed positively to kinetic stability. On the other hand, sequences that did not form rings but had favorable free energy of adsorption (more negative ΔG_{bind}) were kinetically stable. In sum, our work has identified computationally determined parameters and their experimental correlates to better elucidate the structure-function relationship in oligonucleotide-SWNT hybrid systems.

4. Experimental Section

To understand the relationships among conformations, binding affinity and kinetic stability of short oligonucleotides on SWNTs, MD simulations and experiments of short ssDNA and ssRNA polymers on (9,4) SWNTs were performed.

Molecular Dynamics Simulations: Atomistic simulations were conducted to investigate conjugates of (9,4) SWNTs with 10-, 11-, or 12-nucleotide ssDNAs and ssRNAs of different sequences, listed in Table S2 in the Supporting Information, selected in order to examine the effects of several parameters. Nonbase pairing sequences that have different (A,T,C,G) composition, sequences that had the same nucleotide composition but different nucleotide order, and sequences that were different by 1 or 2 nucleotides from the other sequences were selected. The same procedure was used to build the initial structures of conjugates of (9,4) SWNT with the nucleic acids. First, (9,4) SWNT segments, 39 Å in length, were built with VMD software.[42] The initial configurations of ssDNA and ssRNA molecules were built in Material Studio with nucleotides arranged to form helical conformations with radii several Ångstroms wider than the radius of the (9,4) SWNT. The helical DNAs were positioned to wrap SWNTs, with ssDNA bases not pre-adsorbed to the SWNTs surfaces. The prepared ssDNA-SWNT conjugates were solvated with TIP3P water and neutralized with 0.1 M NaCl with solvate and ionize VMD plugins, respectively.[42] The final systems contained approximately 6300 atoms.

The systems were described with CHARMM36 parameters.[43,44] MD simulations were performed with NAMD2.12 package.[45] All simulations were conducted with Langevin dynamics (Langevin constant of 1.0 ps^{-1}) in the NpT ensemble, where temperature and pressure remained constant at 310 K and 1 bar, respectively. The particle-mesh Ewald (PME) method was used to calculate Coulomb interaction energies, with periodic boundary conditions applied in all directions.[46] The time step was set to 2.0 fs. The evaluation of long range van der Waals and Coulombic interactions was performed every 1 and 2 time steps, respectively. After 1000 steps of minimization, solvent molecules were equilibrated for 2 ns around the ssDNA and SWNTs, which were restrained using harmonic forces with a spring constant of 1 kcal mol^{-1} $Å^{-2}$). Next, the systems were equilibrated in 80 ns production MD runs, with restraints applied only on the edge SWNT atoms.

Free Energy Calculations: The free energy landscapes (Figures 1 and 4; Figures S2 and S3, Supporting Information) were obtained through replica exchange MD (REMD) simulation of ssDNA/ssRNA-SWNT systems. All systems were solvated in 3.63 × 3. 63 × 4.92 nm^3 box, containing approximately 6605 atoms. The box contained approximately 1881 water molecules, modeled using the TIP3P model. In addition to Na^+ counterions neutralizing the system, 45 Na^+ and Cl^- ions were included to match the physiological salt concentration in the experimental system. Periodic boundary conditions were imposed in all dimensions, and PME method was used to calculate long-range electrostatics. Additionally, both ends of SWNT were in contact with their periodic images. Energy minimization and 100 ps of heating (NVT) were performed to reach the starting temperature of 310 K. To perform REMD simulations in NVT ensemble, 54 replicas and a 290–727.4 K temperature range were chosen to maintain exchange acceptance ratios

around 25% with 2 ps exchange time. The total REMD simulation times are summarized in Table S1 in the Supporting Information. The simulation time step was 2 fs and trajectories were extracted every 2 ps.

The first 10 000 (20 ns) configurations of room temperature replica were ignored, and the rest of the configurations were analyzed to obtain the free energy landscape. To generate the free energy landscapes shown in Figures 1 and 4 and Figures S2 and S3 (Supporting Information), two independent order parameters of ssDNA structures were calculated from the obtained system configurations: 1) end-to-end distance of ssDNA molecule (the *z*-distance between centers of mass of the first nucleotide and last nucleotide; z coordinate aligns with the long axis of the CNT); and 2) root mean square deviation (RMSD) of phosphorous atoms of the ssDNA backbone, compared to the configuration these atoms have in the ideal left-handed helix of ssDNA/ssRNA wrapping SWNT.

The probability distribution function (P(x,y)) of the two order parameters described above were calculated and combined to generate free energy (F(x; y)) according to the formula

$$\frac{\Delta F(x,y)}{k_B T} = -ln\left(\frac{P(x,y)}{P_{max}}\right) \quad (1)$$

In the above formula, P_{max} is the maximum value of $P(x, y)$. All the free energy landscapes shown were obtained at 300 K by calculating the 2D free energy landscape according to the above formula, where x and y represent the two selected reaction coordinates described above (the end-to-end distance of ssDNA molecule and RMSD of P-atoms).

Data Analysis—Contact Areas: Contact areas between nucleic acids and SWNT were calculated based on the following equation

$$s_{cont.}(t) = \frac{s_{SWNT}(t) + s_{NA-not\ backbone}(t) - s_{SWNT\ or\ NA-notbackbone}(t)}{2} \quad (2)$$

where $s_{SWNT}(t)$ and $s_{NA\ -\ not\ backbone}(t)$ represent solvent accessible surface areas (SASA) of SWNT and nucleic acid atoms except nucleic-acid backbone atoms at time t, respectively. $s_{SWNT\ or\ NA\ -\ notbackbone}(t)$ denotes SASA of a group of atoms including both SWNT and nucleic acid atoms except backbone atoms. The contact areas were calculated separately for all the structures that populate local free energy minima in free energy landscapes obtained at 300 K. The calculations were performed with SASA VMD plugin.[42] In SASA calculations, van der Waals radius of atoms was set to be 1.4 Å.

Data Analysis—Contact Maps: Contact maps of ssDNA residues wrapping SWNT were calculated with MDtraj.[47] The cut-off distance of 0.45 nm was selected for counting the number of residues that were in contact.

Data Analysis—The probability of Observing Ring Conformations in Single Trajectory MD Simulations: To determine the probability of observing ring conformations in single trajectory MD simulations, following parameters were evaluated for all the sequences and for all the time frames 1) the end-to-end distance of ssDNA molecule (the z-distance between centers of mass of the first nucleotide and last nucleotide; z coordinate aligns with the long axis of the CNT) and 2) the root mean square deviation (RMSD) of phosphorous atoms of the ssDNA backbone, compared to the configuration these atoms have in the ideal left-handed helix of ssDNA/ssRNA wrapping SWNT (a single reference structure). 3D scatter plots of the end-to-end distances and the RMSDs for each time frame were prepared and examined. In the analysis, the clusters of points corresponding to ring conformations were defined to have end-to-end distances in the range (–4 to 4 Å) and RMSD > 2.5 Å. The ring conformations were either transient (the points in the scatter plots did not form a defined cluster) or stable (the points in the scatter plot formed a well-defined cluster). For each sequence, the number of points corresponding to ring conformations was summed and divided by the total number of points comprising each trajectory (usually 4000), providing the fractions of time that the molecules assumed ring conformations in the calculated trajectories.

Experimental Studies: ssDNA oligonucleotides were purchased from Integrated DNA Technologies (Standard Desalting) and HiPCo SWNT were purchased from NanoIntegris (Batch #HR27-104). 1 mg ssDNA was mixed with 4 mg SWNT in 1 mL of 0.1 M NaCl solution. The solution was bath sonicated (Branson Ultrasonic 1800) for 15 min and probe-tip sonicated with 3 mm tip (Cole Parmer Ultrasonic Processor) for 10 min at 6 W in an ice bath. The sonicated solution was allowed to equilibrate at room temperature for 30 min. Unsuspended SWNT and other amorphous carbon material was precipitated by centrifuging the sonicated solution at 16 100 g for 60 min. The supernatant was recovered and the concentration of the colloidally stable ssDNA-SWNT was determined with UV–vis measurements (ThermoFisher NanoDrop One) using an extinction coefficient of 0.036 $(mg\ L^{-1})^{-1}\ cm^{-1}$ at 632 nm.[26] For the preparation of ssDNA-Cy5-SWNT, 20×10^{-6} M ssDNA with 3' labeled cyanine-5 (Cy5) was mixed with 1 mg SWNT in 0.01 M phosphate-buffered saline (PBS) and the previous suspension protocol was employed with the following changes: the solution was not bath sonicated and the centrifugation time was decreased to 30 min. The concentration of ssDNA-Cy5-SWNT was determined with UV-Vis measurements with an extinction coefficient of 0.02554 $(mg\ L^{-1})^{-1}\ cm^{-1}$ at 910 nm.[48]

A 5 wt% sodium cholate (SC) solution was prepared in Milli-Q water. ssDNA-SWNT solutions were diluted to 5 mg L^{-1} in 0.1 M NaCl solution and 200 µL aliquots were added to each well of a 96-well well plate. Fluorescence emission spectra from each well was determined with a 10× objective on an inverted Zeiss microscope (Axio Observer.D1) connected to a Princeton Instruments spectrometer (SCT 320) and coupled to a liquid nitrogen-cooled Princeton Instruments InGaAs detector (PyLoN-IR). A 721 nm laser (OptoEngine LLC) produced 80 mW laser power at the back focal plane of the objective for excitation. Spectra were recorded with 1 s exposure time. To obtain temporally resolved evolution of fluorescence shift caused by SC, emission from each well was monitored for 60 s to obtain baseline spectra. To record the fluorescence emission wavelength shift, 4 µL of the 5 wt% SC solution was added to a well as marked by a black arrow in Figure 5b, and SC was allowed to diffuse passively through the well. After SC addition, fluorescence emission spectra was collected for an additional 300 s. All measurements were background corrected with blank 0.1 M NaCl solution.

40 µL of ssDNA-Cy5-SWNT in 0.1 M PBS and 10 µL of SC solution were added to a 96-well PCR plate (Bio-Rad) for a final concentration of 5 mg L^{-1} ssDNA-Cy5-SWNT and 0.1 wt% SC. For control measurements, either ssDNA-Cy5-SWNT was substituted with ssDNA-Cy5 at a final concentration 0.20×10^{-6} M or SC was substituted with 0.1 M PBS. The plate was covered with an optically transparent adhesive seal (Bio-Rad). Cy5 fluorescence was measured with a Bio-Rad CFX96 Real Time qPCR System, scanning all manufacturer set color channels (FAM, HEX, Texas Red, Cy5, Quasar 705) every 30 s at 22.5 °C (no lid heating) for a total of 60 min. Time-resolved fluorescence was analyzed without background correction.[28] Fluorescence-fold increase was calculated by dividing the Cy5 intensity of ssDNA-Cy5-SWNT with SC added by the Cy5 intensity of ssDNA-Cy5-SWNT with PBS.

TEM Imaging: For TEM imaging of $(GT)_6$-SWNT and $(GT)_{15}$-SWNT samples, a FEI ThemIS TEM with 60 kV acceleration voltage was used. An aliquot of 5 µL of $(GT)_6$-SWNT or $(GT)_{15}$-SWNT at a concentration of 10 mg L^{-1} was drop casted onto holey carbon film coated Cu TEM grids, allowed to adsorb for 30 min, and the surface was rinsed. The TEM grid surface was treated with a glow plasma discharger for hydrophilic surfaces. Samples were used directly for TEM imaging without staining.

Supporting Information

Supporting Information is available from the Wiley Online Library or from the author.

Acknowledgements

The authors gratefully acknowledge computer time provided by the Texas Advanced Computing Center (TACC). This research was part of the Blue

Waters sustained-petascale computing project, which was supported by the National Science Foundation (Awards OCI0725070 and ACI-1238993) and the state of Illinois. M.P.L. acknowledges support of a Burroughs Wellcome Fund Career Award at the Scientific Interface (CASI), a Stanley Fahn PDF Junior Faculty Grant with Award # PF-JFA-1760, a Beckman Foundation Young Investigator Award, a DARPA Young Faculty Award, an FFAR New Innovator Award, and a USDA award. M.P.L. is a Chan Zuckerberg Biohub Investigator and an Innovative Genomics Institute Investigator.

Conflict of Interest

The authors declare no conflict of interest.

Keywords

carbon nanotubes, corona phase, molecular dynamics simulations, polymer surface adsorption, ssDNA conformation

Received: February 26, 2020
Revised: April 12, 2020
Published online:

[1] S. Kruss, D. P. Salem, L. Vuković, B. Lima, E. Vander Ende, E. S. Boyden, M. S. Strano, *Proc. Natl. Acad. Sci. USA* **2017**, *114*, 1789.
[2] A. G. Beyene, A. A. Alizadehmojarad, G. Dorlhiac, N. Goh, A. M. Streets, P. Král, L. Vuković, M. P Landry, *Nano Lett.* **2018**, *18*, 6995.
[3] X. He, H. Htoon, S. K. Doorn, W. H. Pernice, F. Pyatkov, R. Krupke, A. Jeantet, Y. Chassagneux, C. Voisin, *Nat. Mater.* **2018**, *17*, 663.
[4] A. Saha, B. J. Gifford, X. He, G. Ao, M. Zheng, H. Kataura, H. Htoon, S. Kilina, S. Tretiak, S. K. Doorn, *Nat. Chem.* **2018**, *10*, 1089.
[5] A. G. Beyene, K. Delevich, J. T. Del Bonis-O'Donnell, D. J. Piekarski, W. C. Lin, A. W. Thomas, S. J. Yang, P. Kosillo, D. Yang, G. S. Prounis, L. Wilbrecht, *Sci. Adv.* **2019**, *5*, eaaw3108.
[6] H. Wan, H. Du, F. Wang, H. Dai, *Adv. Funct. Mater.* **2019**, *29*, 1900566.
[7] J. D. Harvey, R. M. Williams, K. M. Tully, H. A. Baker, Y. Shamay, D. A. Heller, *Nano Lett.* **2019**, *19*, 4343.
[8] C. W. Lin, S. M. Bachilo, Y. Zheng, U. Tsedev, S. Huang, R. B. Weisman, A. M. Belcher, *Nat. Commun.* **2019**, *10*, 2874.
[9] H. Zhang, G. S. Demirer, H. Zhang, T. Ye, N. S. Goh, A. J. Aditham, F. J. Cunningham, C. Fan, M. P. Landry, *Proc. Natl. Acad. Sci. USA* **2019**, *116*, 7543.
[10] Y. Zheng, S. M. Bachilo, R. B. Weisman, *ACS Nano* **2019**, *13*, 8222.
[11] G. S. Demirer, H. Zhang, N. S. Goh, E. González-Grandío, M. P. Landry, *Nat. Protoc.* **2019**, *14*, 2954.
[12] M. J. O'Connell, S. M. Bachilo, C. B. Huffman, V. C. Moore, M. S. Strano, E. H. Haroz, K. L. Rialon, P. J. Boul, W. H. Noon, C. Kittrell, J. Ma, *Science* **2002**, *297*, 593.
[13] C. Richard, F. Balavoine, P. Schultz, T. W. Ebbesen, C. Mioskowski, *Science* **2003**, *300*, 775.
[14] M. Zheng, A. Jagota, E. D. Semke, B. A. Diner, R. S. McLean, S. R. Lustig, R. E. Richardson, N. G. Tassi, *Nat. Mater.* **2003**, *2*, 338.
[15] R. Qiao, P. C. Ke, *J. Am. Chem. Soc.* **2006**, *128*, 13656.
[16] E. L. Bakota, L. Aulisa, D. A. Tsyboulski, R. B. Weisman, J. D. Hartgerink, *Biomacromolecules* **2009**, *10*, 2201.
[17] G. Bisker, J. Dong, H. D. Park, N. M. Iverson, J. Ahn, J. T. Nelson, M. P. Landry, S. Kruss, M. S. Strano, *Nat. Commun.* **2016**, *7*, 10241.
[18] A. Antonucci, J. Kupis-Rozmysłowicz, A. A. Boghossian, *ACS Appl. Mater. Interfaces* **2017**, *9*, 11321.
[19] L. Chio, J. T. Del Bonis-O'Donnell, M. A. Kline, J. H. Kim, I. R. McFarlane, R. N. Zuckermann, M. P. Landry, *Nano Lett.* **2019**, *19*, 7563.
[20] J. D. Harvey, H. A. Baker, M. V. Ortiz, A. Kentsis, D. A. Heller, *ACS Sens.* **2019**, *4*, 1236.
[21] D. P. Salem, M. P. Landry, G. Bisker, J. Ahn, S. Kruss, M. S. Strano, *Carbon* **2016**, *97*, 147.
[22] M. P. Landry, H. Ando, A. Y. Chen, J. Cao, V. I. Kottadiel, L. Chio, D. Yang, J. Dong, T. K. Lu, M. S. Strano, *Nat. Nanotechnol.* **2017**, *12*, 368.
[23] G. Bisker, N. A. Bakh, M. A. Lee, J. Ahn, M. Park, E. B. O'Connell, N. M. Iverson, M. S. Strano, *ACS Sens.* **2018**, *3*, 367.
[24] J. Budhathoki-Uprety, J. Shah, J. A. Korsen, A. E. Wayne, T. V. Galassi, J. R. Cohen, J. D. Harvey, P. V. Jena, L. V. Ramanathan, E. A. Jaimes, D. A. Heller, *Nat. Commun.* **2019**, *10*, 3605.
[25] S. Iliafar, J. Mittal, D. Vezenov, A. Jagota, *J. Am. Chem. Soc.* **2014**, *136*, 12947.
[26] D. P. Salem, X. Gong, A. T. Liu, V. B. Koman, J. Dong, M. S. Strano, *J. Am. Chem. Soc.* **2017**, *139*, 16791.
[27] Z. Li, Y. Song, A. Li, W. Xu, W. Zhang, *Nanoscale* **2018**, *10*, 18586.
[28] R. L. Pinals, D. Yang, A. Lui, W. Cao, M. P. Landry, *J. Am. Chem. Soc.* **2020**, *142*, 1254.
[29] R. Nißler, F. A. Mann, H. Preiß, G. Selvaggio, N. Herrmann, S. Kruss, *Nanoscale* **2019**, *11*, 11159.
[30] D. Roxbury, J. Mittal, A. Jagota, *Nano Lett.* **2012**, *12*, 1464.
[31] A. Shankar, M. Zheng, A. Jagota, *J. Phys. Chem. C* **2017**, *121*, 17479.
[32] J. H. Dwyer, Z. Shen, K. R. Jinkins, W. Wei, M. S. Arnold, R. C. Van Lehn, P. Gopalan, *Langmuir* **2019**, *35*, 12492.
[33] Y. Sugita, Y. Okamoto, *Chem. Phys. Lett.* **1999**, *314*, 141.
[34] R. R. Johnson, A. Kohlmeyer, A. T. C. Johnson, M. L. Klein, *Nano Lett.* **2009**, *9*, 537.
[35] Y. Yang, M. Zheng, A. Jagota, *npj Comput. Mater.* **2019**, *5*, 3.
[36] S. Jeong, D. Yang, A. G. Beyene, J. T. Del Bonis-O'Donnell, A. M. Gest, N. Navarro, X. Sun, M. P. Landry, *Sci. Adv.* **2019**, *5*, eaay3771.
[37] P. Chaturvedi, L. Vuković, *J. Phys. Chem. B* **2019**, *123*, 8216.
[38] M. P. Landry, L. Vukovic, S. Kruss, G. Bisker, A. M. Landry, S. Islam, R. Jain, K. Schulten, M. S. Strano, *J. Phys. Chem. C* **2015**, *119*, 10048.
[39] F. F. Bergler, F. Schöppler, F. K. Brunecker, M. Hailman, T. Hertel, *J. Phys. Chem. C* **2013**, *117*, 13318.
[40] F. Schöppler, C. Mann, T. C. Hain, F. M. Neubauer, G. Privitera, F. Bonaccorso, D. Chu, A. C. Ferrari, T. Hertel, *J. Phys. Chem. C* **2011**, *115*, 14682.
[41] P. V. Jena, M. M. Safaee, D. A. Heller, D. Roxbury, *ACS Appl. Mater. Interfaces* **2017**, *9*, 21397.
[42] W. Humphrey, A. Dalke, K. Schulten, *J. Mol. Graphics* **1996**, *14*, 33.
[43] E. J. Denning, U. D. Priyakumar, L. Nilsson, A. D. Mackerell Jr., *J. Comput. Chem.* **2011**, *32*, 1929.
[44] K. Hart, N. Foloppe, C. M. Baker, E. J. Denning, L. Nilsson, A. D. MacKerell Jr., *J. Chem. Theory Comput.* **2012**, *8*, 348.
[45] J. C. Phillips, R. Braun, W. Wang, J. Gumbart, E. Tajkhorshid, E. Villa, C. Chipot, R. D. Skeel, L. Kale, K. Schulten, *J. Comput. Chem.* **2005**, *26*, 1781.
[46] T. Darden, D. York, D. L. Pedersen, *J. Chem. Phys.* **1993**, *98*, 10089.
[47] R. T. McGibbon, K. A. Beauchamp, M. P. Harrigan, C. Klein, J. M. Swails, C. X. Hernández, C. R. Schwantes, L. P. Wang, T. J. Lane, V. S. Pande, *Biophys. J.* **2015**, *109*, 1528.
[48] J. Zhang, M. P. Landry, P. W. Barone, J. H. Kim, S. Lin, Z. W. Ulissi, D. Lin, B. Mu, A. A. Boghossian, A. J. Hilmer, A. Rwei, A. C. Hinckley, S. Kruss, M. A. Shandell, N. Nair, S. Blake, F. Sen, S. Sen, R. G. Croy, D. Li, K. Yum, J.-H. Ahn, H. Jin, D. A. Heller, J. M. Essigmann, D. Blankschtein, M. S. Stran, *Nat. Nanotechnol.* **2013**, *8*, 959.

